Prediction of Cavitation Performance of Radial Flow Pumps

M. Kaya[1,2,†] and E. Ayder[2]

[1]R and D Department, Standart Pompa A.S., Istanbul, Turkey
[2] Mechanical Engineering Department, Istanbul Technical University, Istanbul, Turkey

†*Corresponding Author Email: mkaya@standartpompa.com*

ABSTRACT

Cavitation is a major problem in pump design and operation because this phenomenon may lead to various types of instabilities, including hydraulic performance loss and catastrophic damage to the pump material caused by bubble collapse. Therefore, it is critical to predict the cavitation performance of the pump in the design phase itself. The motivation of this study is to develop a systematic methodology to calculate the cavitation performance of radial flow pumps. In the first step of the present work, a cavitating nozzle flow case for which the bubble dynamic behavior is accurately resolved in literature is studied numerically. Subsequently, the capabilities of three cavitation models, implemented in the commercial code Fluent, are evaluated for three radial flow pumps designed at specific speeds n_s = 10.4, 22.4, and 34.4. The numerical results are validated with global quantities based on net positive suction head (NPSH) measurements. The results led to the determination of reasonably accurate NPSH values for the defined range of specific speeds.

Keywords: NPSH; Cavitation; Pump; Bubble dynamics.

NOMENCLATURE

b_2	impeller outlet width	P	local pressure
C_p	pressure coefficient	P_{01}	inlet total pressure
D_0	impeller eye diameter	P_v	vapor pressure
D_2	impeller outlet diameter	P_s	inlet pressure
f_g	non-condensable gas mass fraction	Q	flow rate
f_v	vapor mass fraction	R_B	bubble radius
H	pump head	u_s	inlet velocity
k	turbulent kinetic energy		
n	impeller rotation speed	β_2	blade outlet angle
n_s	specific speed	ρ	density
NPSH	net-positive suction head	σ_n	cavitation number

1. INTRODUCTION

Conventionally, the cavitation performance of a centrifugal pump is associated with a critical value called net positive suction head required, $NPSH_r$. It is the difference between the absolute total pressure at the plane of impeller inlet and vaporization pressure. When handling this critical value, there are several alternatives such as the cavitation inception value $NPSH_i$, or developed cavitation values like $NPSH_3$ or $NPSH_5$. When calculating $NPSH_3$, inlet conditions are used at the state when the pump head is reduced by 3% owing to the effects of the cavitated

flow field compared to a non-cavitating case at the same flow rate.

Pump manufacturers conventionally declare $NPSH_3$ values in their catalogues for practical reasons. To determine the $NPSH_i$ value, the visual inception of bubbles has to be captured by optical measurements. However, this procedure is highly expensive to be repeatedly performed for a family of pumps. Furthermore, this value is much higher than the $NPSH_3$ value, making it difficult for the installers to provide an adequate NPSH in several cases. Some developed cavitation is therefore, usually allowed on site. The limit is set to the 3% head drop case and is

fixed by international standards. In this manner, it becomes possible to calculate the NPSH value by simple static pressure measurements.

In this perspective, the main purpose of this study is to estimate the NPSH$_3$ value of end-suction radial flow pumps at the design phase via numerical calculations. The successful estimation of NPSH$_3$ will provide an opportunity to analyze the effects of geometric parameters on the cavitation performance of pumps. Furthermore, it will lead to the development of a design methodology for low NPSH$_3$ radial pumps.

In recent years, numerical modeling of cavitation has been used effectively in academia as well as industry. Cavitation models are generally categorized into 3 groups: barotropic models, interface tracking models, and bubble dynamic models. NPSH calculations are possible with all these models.

Visser (2001) used the CFX CEV barotropic model to calculate the head-drop and Q-NPSH$_3$ curves. This model yielded good results particularly at optimum and partial flow rates compared to experiments. This model was also used by Nohmi (2012) in a three-vane, low specific speed pump. As before, the calculated head-drop curve was found to be consistent with experimental results at the optimum flow rate, but the gradual head-drop at higher flow rates could not be captured.

Surface tracking methods resolve the interface between the vapor cavity and surrounding fluid and iteratively adapt the cavity shape. For the theoretical background in this regard, refer the work of Hirschi et al. (1998). Dupont (2001) used the surface tracking model to calculate the cavitating flow field in pumps. The calculated and measured cavity lengths showed good agreement. Another example of this method is the work of Li et al. (2006) in which the cavity thickness and pressure coefficient distribution along blade surfaces were computed.

Bubble dynamic models employ simplified forms of the Rayleigh–Plesset equation to calculate the cavitated flow field. Source terms in the transport equation for the volume fraction are modeled, considering the evaporation and condensation processes. Niedzwiedzka et al. (2016) gave a detailed overview of the available models that can be used with homogenous approach. These models are generally validated with hydrofoil, venturi, or cylinder test cases. Amongst these, the models of Zwart et al. (2004), Schnerr and Sauer (2001), and Singhal et al. (2002) hereafter referred to as the Zwart, Schnerr, and Singhal models are the most frequently used models for the hydrodynamic cavitation in pumps and inducers. The bubble dynamics approach is already implemented in commercial CFD packages such as Fluent and CFX. The model proposed by Zwart is the default model in CFX and has been used in its original form by Balasubramanian et al. (2011), Shukla et al. (2008), Somashekar et al. (2012), and Jeanty et al. (2009) for centrifugal pump applications. Marini et al. (2011) studied impeller cavitation using the models of Zwart and Schnerr with the Fluent software and reported the Schnerr model as the more accurate one.

This model is presently the default option in Fluent. There are also successful applications of the Singhal model for the head-drop curve calculation such as that by Li (2014) using Fluent. Ding et al. (2011) also adopted this model into the Pumplinx CFD tool, which gave good estimations of the NPSH$_i$ curve.

As explained above, there are several published studies in this field. On the other hand, the present study covers a wide range of specific speeds over their allowable operating ranges. Three end-suction radial pumps designed for n_s = 10.4, 22.4, and 34.4 were selected. The cavitation models proposed by Zwart, Schnerr, and Singhal were considered, and their capabilities were evaluated for end-suction radial flow pumps.

In this article, initially, the theoretical background of cavitation models is provided. Then, in the first part, the effects of the simplifications over the Rayleigh-Plesset equation are investigated on a converging–diverging nozzle case. In the second part, the cavitating flow in radial pumps is analyzed. The experimental setup and measurement methodology is briefly explained. After that, three-dimensional (3D) cavitating pump calculations are performed. For the pump with n_s = 34.4, cavitation is calculated in a single impeller passage as well as in a more realistic model, including all rotating and stationary elements. The effect of the calculation domain extension with volute casing and leakage zones on the NPSH value is analyzed. Furthermore, the effects of inlet and outlet boundary conditions (BCs) on the head-drop characteristics are evaluated. The same numerical procedure is repeated for other pumps. Numerical results are compared with experimental values based on NPSH measurements.

2. CONSERVATION EQUATIONS AND CAVITATION MODELS

A two-phase flow of water and water vapor is considered. The commercial code Fluent is used to calculate the cavitational flow in a one-dimensional (1D) nozzle and in radial flow impellers. Continuity, momentum, and volume fraction equations are solved with the homogeneous mixture approach. The velocity slip between phases is not considered. Body forces and heat transfer are neglected. The set of equations is given below. Because the computations are in steady state, all transient terms drop.

$$\frac{\partial \rho_m}{\partial t} + \frac{\partial(\rho_m u_j)}{\partial x_j} = 0 \tag{1}$$

$$\frac{\partial(\rho_m u_i)}{\partial t} + \frac{\partial(\rho_m u_i u_j)}{\partial x_j} = -\frac{\partial P}{\partial x_i} \tag{2}$$

$$+ \frac{\partial}{\partial x_j}\left[(\mu_m + \mu_T)\left(\frac{\partial u_i}{\partial x_j} + \frac{\partial u_j}{\partial x_i} - \frac{2}{3}\frac{\partial u_k}{\partial x_k}\delta_{ij}\right)\right]$$

$$\frac{\partial(\rho_v \alpha_v)}{\partial t} + \frac{\partial(\rho_v \alpha_v u_j)}{\partial x_j} = \dot{m}^- - \dot{m}^+ \tag{3}$$

$$\rho_m = \rho_v \alpha_v + \rho_l \alpha_l \tag{4}$$

$$\mu_m = \mu_v \alpha_v + \mu_l \alpha_l \tag{5}$$

Here, ρ_m is the mixture density, ρ_l is the density of water, ρ_v is the density of water vapor, α_v is the volume fraction of vapor, α_l is the volume fraction of water, μ_m is the laminar viscosity of the mixture, μ_l and μ_v are the liquid and vapor dynamic viscosities, respectively, and μ_t is the turbulent viscosity. Source terms $\dot{m}^-$ and $\dot{m}^+$ in the volume fraction equation are the interphase mass transfer rates per unit volume for the vaporization and condensation processes, respectively. These source terms are derived using simplified forms of the Rayleigh–Plesset equation for bubble dynamics. The general form of the equation is

$$\frac{P_v - P}{\rho_l} = R_B \frac{d^2 R_B}{dt^2} + \frac{3}{2}\left(\frac{dR_B}{dt}\right)^2 + \frac{4\vartheta_L}{R_B}\frac{dR_B}{dt} + \frac{2\sigma}{\rho_l R_B} \quad (6)$$

This equation expresses the growth and collapse of a bubble of radius R_B. Elimination of the surface tension term, viscous term, and 2nd order derivative for the acceleration term leads to the basic expression given below. This simplification is used in all the cavitation models considered in this study.

$$\frac{dR_B}{dt} = \sqrt{\frac{2}{3}\left(\frac{P_v - P}{\rho_l}\right)} \quad (7)$$

The above expression allows the introduction of bubble dynamic effects into the transport equation for mass transfer. A brief overview of the source terms in the Zwart, Schnerr, and Singhal models are as follows:

Zwart Model (2004)

$$\dot{m}^- = F_{Vap}\frac{3\alpha_{nuc}(1 - \alpha_v)\rho_v}{R_B}\sqrt{\left(\frac{2}{3}\frac{P_v - P}{\rho_l}\right)}, P < P_v \quad (8)$$

$$\dot{m}^+ = F_{con}\frac{3\alpha_v\rho_v}{R_B}\sqrt{\left(\frac{2}{3}\frac{P - P_v}{\rho_l}\right)}, P > P_v \quad (9)$$

The evaporation and condensation terms are proportional to the square root of the difference between the local pressure and vapor pressure. F_{vap}, F_{con}, α_{nuc}, and R_B are the model coefficients that should be selected in conformity with the physics of the problem.

Schnerr Model (2001)

$$\dot{m}^- = \frac{\rho_v\rho_l}{\rho}\alpha_v(1 - \alpha_v)\frac{3}{R_B}\sqrt{\left(\frac{2}{3}\frac{P_v - P}{\rho_l}\right)}, \quad P < P_v \quad (10)$$

$$\dot{m}^+ = \frac{\rho_v\rho_l}{\rho}\alpha_v(1 - \alpha_v)\frac{3}{R_B}\sqrt{\left(\frac{2}{3}\frac{P - P_v}{\rho_l}\right)}, \quad P > P_v \quad (11)$$

The only parameter to be specified in this model is the number of bubbles per volume of liquid, n_b, which is not explicitly seen above.

Singhal Model (2002)

$$\dot{m}^- = F_{vap}\frac{\max(1, \sqrt{k})\left(1 - f_v - f_g\right)}{\sigma}\rho_l\rho_v \quad (12)$$
$$\sqrt{\left(\frac{2}{3}\frac{P_v - P}{\rho_l}\right)}, \quad P < P_v$$

$$\dot{m}^+ = F_{con}\frac{\max(1, \sqrt{k})f_v}{\sigma}\rho_l\rho_v\sqrt{\left(\frac{2}{3}\frac{P_v - P}{\rho_l}\right)}, \quad P > P_v \quad (13)$$

Unlike the Zwart and Schnerr models, the Singhal model takes into account the effects of surface tension, turbulent pressure fluctuations, and non-condensable gases. Inclusion of non-condensable gases results in a real advantage when using this model because in real pumping applications, small fractions of air may penetrate inside the pumped media. Furthermore, two-phase mixture is considered to be compressible. F_{vap} and F_{con} are constants.

3. CAVITATING FLOW IN A 1D NOZZLE

A 1D converging–diverging nozzle case is studied before proceeding to the complex pump problem, because exact solutions for the bubble dynamic equations in a 3D geometry are not known yet. In contrast, the bubble dynamics solution of a 1D cavitating nozzle problem as shown in Fig. 1, has been provided by Wang and Brennen (1998). The objective of this calculation is to determine whether the pressure drop due to the cavitation and vaporization zones are determined appropriately with the selected cavitation models. In this context, turbulence and boundary layer effects are not involved. Furthermore, we intend to study the effects of the simplifications of the Rayleigh–Plesset equation when using cavitation models.
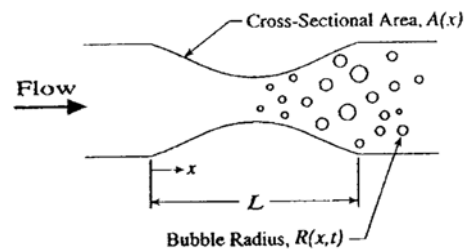

Fig. 1. Bubbly flow in the nozzle, Wang and Brennen (1998).

Wang and Brennen (1998) solved the dimensionless continuity, momentum, and Rayleigh–Plesset equations in steady state. Turbulence is not involved. A fluid composed of liquid water and air bubbles of radius 100 μm enters the nozzle with a 10 m/s inlet velocity and at a cavitation number of $\sigma_n = 0.8$. The minimum pressure coefficient at the throat (x/0.5L) is selected as -1 to ensure cavitation $(\sigma < -C_{pmin})$. An effective liquid viscosity of $\mu e = 0.03$ Ns/m^2 is considered to incorporate various bubble damping

mechanisms. Five different upstream void fractions α_s of the order 10^{-6} are considered. $\alpha_s = 0$ corresponds to the case without bubbles studied by Wang and Brennen (1998).

In the present study, numerical analysis of single-phase and two-phase flows is performed in a 2D computational domain. The domain is meshed with 50 structured mesh elements perpendicular to the flow and 300 elements parallel to the flow. The void fraction equation is solved instead of the Rayleigh–Plesset equation. The material properties of water vapor are specified based on the given temperature at the saturation condition. The following two different values are used for the vapor density: 0.0094 kg/m³ at 10 °C and 0.023 kg/m³ at 25 °C. A laminar flow with free slip at the walls is considered. First, single-phase water flow is solved corresponding to the $\alpha_s = 0$ case. Then the two-phase cavitating flow is solved with an inlet void fraction of 2.5×10^{-6}. Because the same simplifications are applied to all the cavitation models, only the Zwart model is used for the nozzle calculations for demonstration purposes. A 100-µm of initial bubble radius is imposed. A convergence criterion of 10^{-5} is set for the continuity, momentum, and volume fraction equation residuals. Comparative solutions of pressure coefficient and volume fraction along the flow direction are shown in Fig. 2.
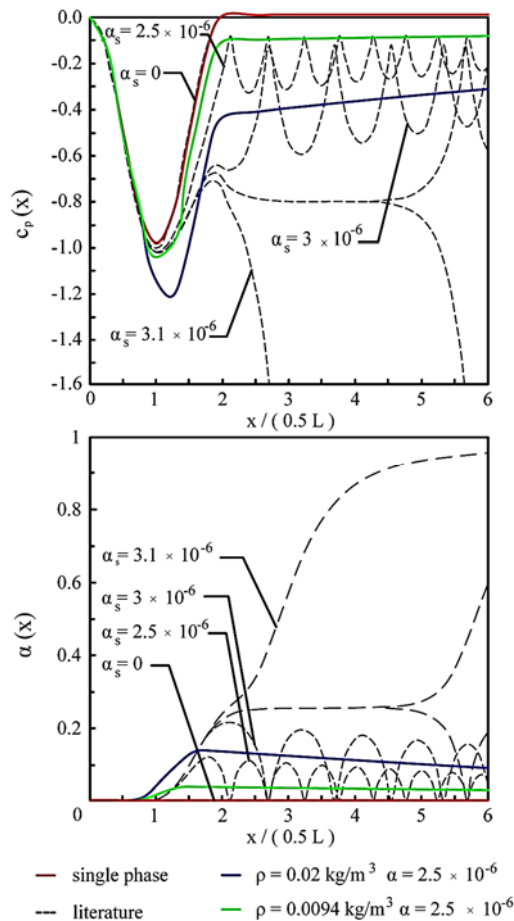
Considering the single-phase flow case, there is a negligible pressure drop similar to the results of Wang and Brennen (1998). This small loss is only because of friction and viscosity. For the cavitating flow case with $\rho_v = 0.0094$ kg/m³, the pressure field changes dramatically even at very low levels of the inlet void fraction. When the density of the vapor is increased to $\rho_v = 0.023$ kg/m³, the pressure loss becomes more. This loss is only a result of the growth of bubbles after the throat area and can be defined as the cavitation loss. Variation of the vapor density as the temperature is changed from 10 °C to 25°C modifies the pressure field drastically. Thus, for multiphase calculations, temperature of the vapor phase should be precisely designated. Solutions for different α_s are provided in the literature. Because the α_s variation is very small, only $\alpha_s = 2.5 \times 10^{-6}$ is considered in the present study.

As seen from Fig. 2, averaged profiles of C_p and α are achieved. In contrast, the oscillatory behavior of bubbles could not be captured, possibly owing to the elimination of the second order derivative term from the original Rayleigh–Plesset equation. However, global quantities such as the pressure drop due to cavitation are approximately computed, which is the main motivation of NPSH computations for pumps.

4. CAVITATING FLOW IN RADIAL PUMPS

Meridional views of the selected impellers, all scaled to the same outlet diameter, are shown in Fig. 3.
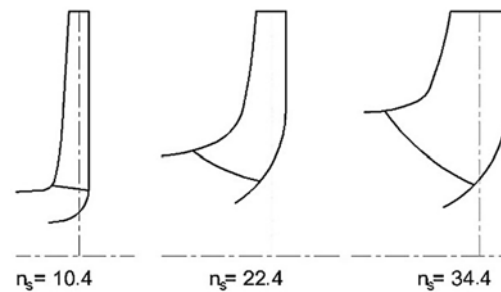

Fig. 3. Meridional view of selected radial impellers.

Some of the characteristic features of these selected pumps are listed below. The $n_s = 10.4$ pump has cylindrical blades, while the other impellers have blades of double curvature.

Table 1 Some characteristic dimensions of the selected impellers

	$n_s = 10.4$	$n_s = 22.4$	$n_s = 34.4$
D_2 [mm]	328	179	177
b_2 [mm]	13,5	10.8	21
D_0 [mm]	87	73	105
number of blades	4	5	6
$\beta2$ [°]	28	26	25

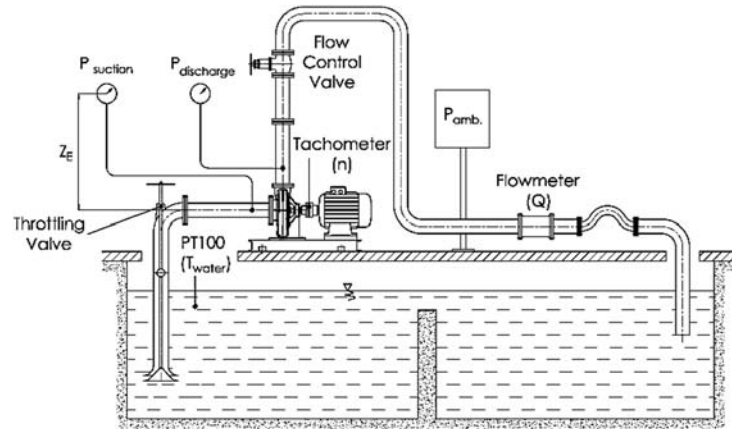**Fig. 2. Literature and current results for C_p and α along the flow axis.**

Fig. 4. Schematic of the test rig.

4.1 Experimental Setup and Determination of Pump Characteristics

The experiments were conducted at the open loop test rig of Standart Pompa AS. A schematic of the test bench is presented in Fig. 4. Performance measurements were realized by fulfilling the requirements of the rotodynamic pumps— hydraulic performance acceptance tests— ISO EN 9906 standard. All the data acquisition systems, measurement methods, and equipment calibration were according of international standards. As can be seen from Fig. 4, a suction pool of 400 m³ capacity is used in the performance tests, which is filled with fresh water. Prior to running, air is evacuated from the suction line with a vacuum pump. When the pumps are filled with water, operation is initiated using a soft starter connected to a three-phase electric motor in synchronous speed. The suction line is equipped with a throttling valve to control the suction pressure. The pipeline characteristics and pump flow rate are determined through a flow control valve placed at the discharge line. The discharged water flows through a magnetic flowmeter and is flushed back into the pool afterwards.

The volumetric flow rate is measured with different sizes of flowmeters based on the pump capacity. The suction pressure is obtained from an absolute pressure transducer, while the discharge pressure is determined using two different sizes of gauge pressure transducers based on the pump outlet pressure levels.

Atmospheric pressure measurement is also required to bring the suction and discharge pressure readings on the same level. This is accomplished using an air station. The rotation speed is measured with a laser tachometer from the pump shaft. The temperature of water is measured with a thermocouple placed at the sump, near the suction pipeline. This is used to determine the density of water and vaporization pressure.

Digital data from the measurement chain are collected in the data acquisition system, which is controlled with a sophisticated software. A list of equipment, their accuracy, and max. uncertainty associated with the calculated quantities are provided in Table 2 and Table 3.

Table 2 Accuracy of measurements

Measured quantity	Equipment	Accuracy
Q	Krohne - Optiflux DN50	± 0.5%
	Krohne - Optiflux DN80	± 0.5%
	Krohne - Optiflux DN125	± 0.5%
$P_{suction}$	Keller - PAA33X - 3bar$_A$	± 0.05%
$P_{discharge}$	Keller - PR33X -3bar.g	± 0.05%
	Keller - PR33X -10bar.g	± 0.05%
$P_{ambient}$	Delta OHM - HD2001.1	± 0.1%
n	UNI-T - UT372	± 0.02%
T_{water}	PT100	-

Table 3 Uncertainties for head and NPSH₃

Calculated results	Uncertainty
H	± 1.5%
NPSH$_3$	± 1.5%

To determine the Q-NPSH$_3$ characteristics, Q–H performance curves should be known first. Therefore, performance tests for three pumps are conducted at a constant speed in a fully open inlet valve position, allowing for the highest inlet pressure. Performance curves for all the pumps are constructed over their operating ranges. For the cavitation tests, the throttling valve at the suction pipeline is gradually closed to achieve the desired pressure loss. To compensate for the reduction in flow, the discharge valve is further opened to fix the

flow rate. When the pump head is reduced by 3% compared to the non-cavitating conditions at the same flow rate and speed, the suction pressure measurements are used to calculate the $NPSH_3$ value.

$$NPSH_3 = \frac{P_{suction}}{\rho g} + \frac{V_{suction}^2}{2g} - p_v + z_e \qquad (14)$$

Here, z_e is the elevation difference between the measurement plane and NPSH datum plane, and $V_{suction}$ is the axial velocity at the suction pipe measurement section.

NPSH measurements for three pumps are performed over the allowable operating ranges of the pumps.

Table 4 Mesh independence analysis for passage and full model calculations of $n_s = 34.4$ pump

$n_s = 34.4$ passage calculations [structured hex. elements]			
	coarse	medium	fine
inlet mesh size	31020	74340	168168
passage mesh size	107734	248730	689346
outlet mesh size	93060	282000	670320
y^+ on blades min–max	1.3-15	0.9-15	0.9-14
y^+ area average value on blades	12.8	12.2	10.8
H [m]	36.93	37.12	37.2
$n_s = 34.4$ full model calculations [unstructured tetra. elements]			
	coarse	medium	fine
suct. chamber mesh size	122712	237393	354781
impeller mesh size	1638554	2410392	3851258
volute casing mesh size	2070328	3486031	4215952
y^+ on blades min–max	8.3-383	2.4-314	0.4-208
y^+ area average value on blades	285	130.6	102
H [m]	37.1	37.02	37.08

4.2 Cavitation Performance Analysis of $n_s = 34.4$ Pump

First, computations are conducted for the $n_s = 34.4$ pump. All pump components, including the suction chamber, volute casing, sidewalls, leakage zones with gaps on the front and back wear rings, balance holes, and seal flush are modeled, as shown in the mesh section view in Fig. 5.

The calculation domain is decomposed into 39 parts. The inlet and outlet pipes are added to the model to enable a homogenous boundary condition (BC) imposition. Unstructured tetragonal elements are used to mesh the domain, as can be seen from Fig. 6.
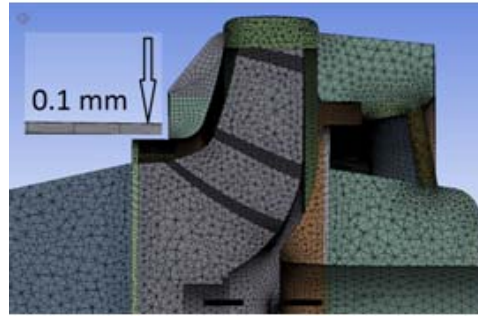

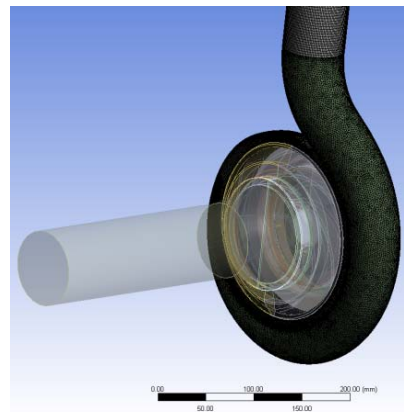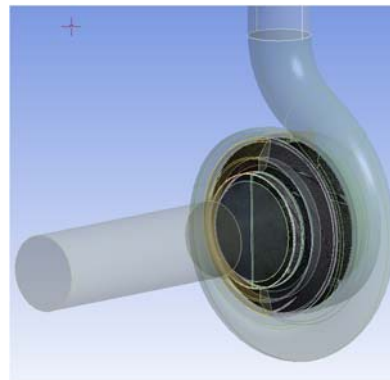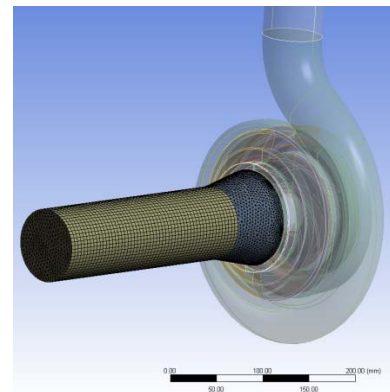**Fig. 5. Details from the gap (100 μm) below the front wear ring.**

Fig. 6. Computational domain of $n_s = 34.4$ pump; inlet elements, impeller, and volute casing.
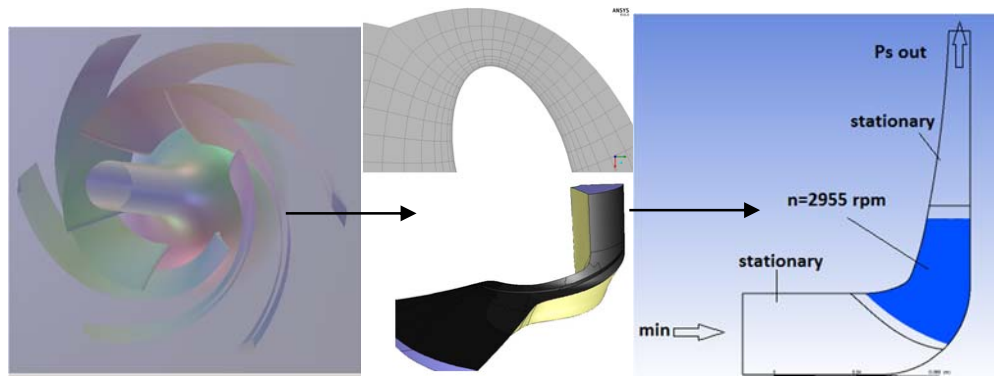
Fig. 7. Passage flow calculation steps for $n_s = 34.4$ pump.

Single-phase solutions are obtained with a steady state approach using the moving reference frame (MRF) scheme for the impeller. Inlet mass flow rate and outlet static pressure boundary conditions are prescribed. Turbulence is modeled with the realizable k–ε model together with scalable wall functions. This type of wall functions enables the usage of arbitrarily fine mesh. For grid refinements below $y^+ < 11$, deterioration in the standard wall functions is avoided. For a coarser mesh, standard wall functions are identical where the centroid of the wall-adjacent cell is located within the logarithmic law layer, i.e., $30 < y^+ < 300$. After that, the flow field at one passage of the impeller is studied. Inlet and outlet of the passage are extended as well, with the principle of zero diffusion. The mesh is constructed with structured hexagonal elements. Details from the leading edge are shown in Fig. 7. Because there is leakage from the front wear ring gap, back ring gap, seal flush, and balance holes, the flow rate passing through the impeller is higher than that at the pump outlet. The leakage is calculated using empirical correlations and added to the pump inlet flow rate. Based on the calculated leakage rates, the volumetric efficiency is 97.1% at $Q/Q_{opt} = 1.16$, 96.6% at $Q/Q_{opt} = 1.05$, and 96.08% at $Q/Q_{opt} = 0.95$ where Q_{opt} stands for the flow rate at the best efficiency point (BEP). Single-phase computations are repeated under periodic BCs using the MRF scheme. A convergence criteria of 10^{-5} is set for continuity, momentum, and turbulence equation residuals.

A mesh independence study is performed at the $Q = 1.05Q_{opt}$ operating point flow rate for the single-phase flow. Table 4 summarizes the mesh information and calculated head values in each simulation step.

Regarding passage calculations, refining the mesh from coarse to fine resulted in an increased head value of 0.5% and 0.2% in each step. First, the node height is reduced until 3.7 microns in the fine mesh case, while only a minor change resulted in the area average value of y^+. Therefore, further refinement is not considered and a medium size mesh is found sufficient. For full model calculations, a coarse mesh is selected because negligible head variation is observed with a finer mesh. Although a large value of y^+ is observed in full model calculations, the criteria for logarithmic law layer is satisfied.

The pump head is calculated for three operating points for $Q/Q_{opt} = 1.16$, 1.05, and 0.95. An overview of the calculation steps for a single passage case is provided in Fig. 7.

The calculated value of H for both the single passage and full model cases at $Q/Q_{opt} = 1.05$ is 37.1 m. Losses in the volute casing are tolerated with the transfer of high-momentum liquid from the impeller sidewalls to the outlet section. The calculation error in the numerical results of H is ~+4% based on the experimental values. Next, the two-phase cavitation calculations for the same pump at the optimum flow rate were performed. The density and viscosity of water vapor were defined at 25 °C. The Zwart model was selected to compare the passage flow and full model cases for $Q/Q_{opt} = 1.05$. The vaporization pressure was set to 3574 Pa and 1 μm was specified as the bubble radius size. A mass flow inlet with zero vapor volume fraction ($\alpha_v = 0$) was imposed. At the outlet, first a high static pressure was imposed to have limited cavitation that would not result in a head-drop. Then, the outlet pressure was gradually reduced stepwise to enhance the cavitation and obtain the head-drop (H–NPSH) curves. The rotation speed and mass flow rate were kept constant. A convergence criteria of 10^{-4} was set for the volume fraction equation residuals. Both for the passage flow and full model cases, steep head-drop characteristics were obtained with a head breakdown value of ~2 m. The H–NPSH curves are given in Fig. 8.

A lower $NPSH_r$ is expected for the full model case because high-pressure liquid flashes into the suction chamber from the balance holes. However, no significant effect on the head-drop curve is observed. Based on this argument, a single passage is used for all other computations. Cavitation calculations near the BEP are also conducted using the Schnerr and Singhal models. For the Schnerr model, $n_b = 10^{13}$ is imposed. For the Singhal model, a non-condensable gas mass fraction of 2.3×10^{-5} is considered. This rate of gas content is specified in order to duplicate the fluid in the experiments. Based on Henry's law, air dissolved in water at 25 °C and 1 atm absolute pressure is calculated to be 0.023 g/kg. This rate is considered constant for all the cases. Steep head-
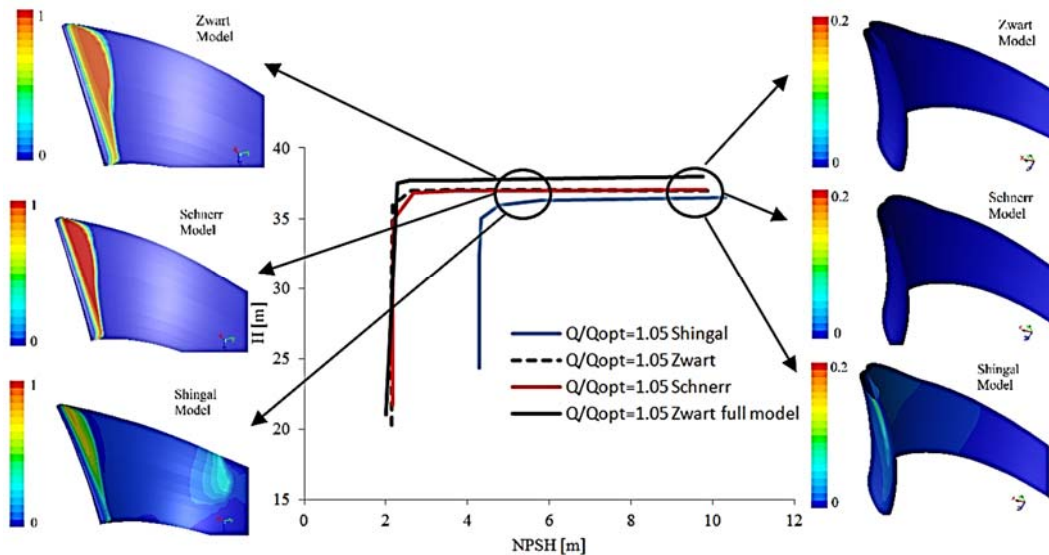
Fig. 8. Head-drop curves for n_s = 34.4 pump and contours of vapor volume fraction on the blades.

drop curves are also obtained with these models. Pump breakdown occurs at a significantly high NPSH in the computations with the Singhal model. The calculation error in the Singhal $NPSH_3$ value is computed to be only -3.5%, based on experimental data.

At high inlet pressures, near NPSH = 10 m, no vapor formation is found to occur using the Zwart and Schnerr models as depicted in Fig. 8. In contrast, a small amount of vapor (0.2 max.) around the suction and discharge sides of the blade leading edge are computed with the Singhal model. Until the cavity length exceeds a certain level, a head-drop owing to cavitation should not occur. As expected, such limited cavity zones do not result in a head-drop in this case. When the NPSH is reduced to 4.4 m, the leading-edge neighborhood is fully occupied by large vapor pockets for all the models. Similar cavity forms develop near the leading edge. There is a larger vapor region around the leading-edge shroud than at the hub because of the higher tangential velocity. Although a considerable amount of vaporization is predicted, the Zwart and Schnerr models do not yield any head-drop in opposition to the Singhal model. This is because the vaporization occurs from the blade to the blade throat and penetrates downstream using the Singhal model. This condition leads to a sudden head-drop even if the volume fraction is lower (0.77 max.) than that for the Zwart and Schnerr models (0.99 max.), as seen from Fig. 8.

The best approximation to the experimental data is obtained using the Singhal model at the maximum efficiency operating point. Consequently, off-design calculations are conducted only with the Singhal model.

4.2.1 Effect of Inlet and Outlet Boundary Conditions

To analyze the effects of inlet and outlet BCs, mass flow inlet type BC is changed to total pressure inlet and static pressure outlet type BC is changed to mass flow outlet. When a mass flow BC is prescribed, mass flow rate for each phase shall be specified separately. This a priori knowledge is only available at pump inlet, where it is known that vaporization is not present. Mass flow rate is kept same for two cases. Resulting velocity distributions at inlet and outlet are shown in Fig. 9. Circumferentially averaged velocity profiles near 3% head drop conditions of Singhal model are plotted for the $1.05Q_{opt}$ operating point. A uniform velocity profile at inl*et al*ong the span is computed for both cases. At the outlet, domain is extended sufficiently to eliminate the effects of a fixed constant static pressure BC around the circumference. Therefore, a slight variation of outlet velocity profiles is observed between two BC sets.
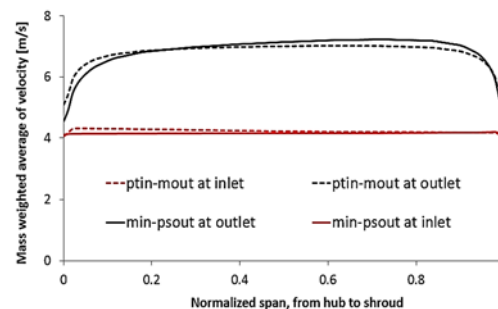

Fig. 9. Velocity distributions at inlet and outlet using two different type of BC sets.

With P_{tin}-m_{out} type of BC set, unrealistic head drop curves are calculated using Singhal model, which produce very gradual head drop characteristics. This is valid for all operating points. The head-drop curves are displayed in Fig. 10. Therefore, m_{in}-P_{sout} type BC set is used for all the subsequent

calculations, which give steeper head drop characteristics as expected. On the other hand, head drop curves are unchanged for Zwart and Schnerr models with modified BC set, therefore are not shown here.
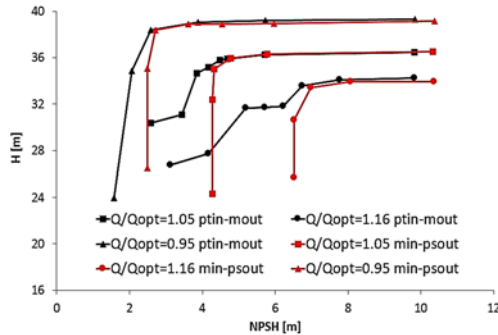

Fig. 10. Head-drop curves over the operating range of n_s = 34.4 pump using the Singhal model.

The Q-NPSH$_3$ curves are generated using the head-drop curves of the Singhal model and compared to experimental data, as seen in Fig. 11. The calculated NPSH3 values are consistent with experimental results near the optimum and overload operating points. However, there is a -27% calculation error at the part-load operating point where the absolute difference in NPSH3 is 0.99 m.
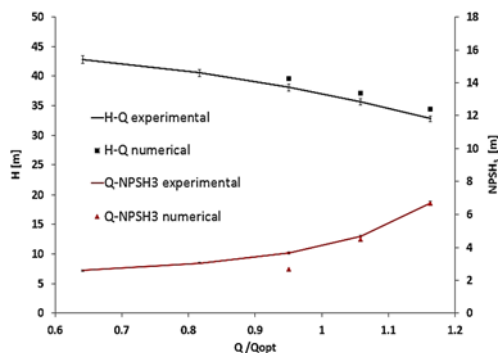

Fig. 11. Q-H and Q-NPSH$_3$ curves for n_s = 34.4 pump obtained numerically and experimentally.

4.3 Cavitation Performance Analysis of n_s = 22.4 Pump

The numerical procedure described earlier is repeated for other pumps. In this context, a mesh independence study is performed for single-phase calculations of the n_s = 22.4 pump at the optimum flow rate. The mesh information is given in Table 5.

Structured hexagonal elements are used. Increasing the mesh element size from coarse to medium resulted in a 1.4% reduction in the head. Refining the mesh further resulted in a 0.5% variation. Although the first node distance is reduced until 28 microns with the fine mesh case, it is seen that the average y^+ on blades is not reduced any further. In this view, a medium sized mesh is selected.

Table 5 Mesh convergence analysis of n_s = 22.4 pump

|	coarse	medium	fine
inlet mesh size	19890	51600	79650
passage mesh size	102408	210872	423252
outlet mesh size	95880	208120	334800
y^+ on blades min-max	1.6-34	1.07-19	1.2-14
y^+ area average value on blades	16.2	11.9	11.7
first node from wall [µm]	70	40	28
H [m]	39.61	39.04	39.22

Head-drop curves are obtained using three cavitation models at the best efficiency operating point. NPSH3 values at BEP are calculated to be higher with the Singhal model than the other models, as seen from Fig. 12a. Furthermore, full cavitation breakdown occurs at higher NPSH values obtained with this model. Steep head-drop characteristics are calculated with all the models. Closest results to NPSH3 measurements at BEP (refer Fig. 12b), are obtained using the Singhal model. Therefore, off-design cavitation calculations at Q/Q_{opt} = 0.76 and 1.19 are performed only with this model. Head-breakdown is predicted at a higher NPSH value for the overload point and at a lower NPSH value for the part load point compared to BEP. Q–NPSH3 curves are constructed based on the head-drop curves. The comparative results are presented in Fig. 12b. The NPSH3 calculation error is -31%, -34%, and -10% for partload, BEP, and overload operating points, respectively. Although the calculated error is not small, the difference is not larger than 1.2 m at any of the operating points.

## 4.4 Cavitation Performance Analysis of n_s = 10.4 Pump

Calculation results for the mesh convergence study of n_s = 10.4 pump are listed in Table 6.

Table 6 Mesh convergence analysis of n_s = 10.4 pump

	coarse	medium	fine
inlet mesh size	24480	37800	55500
passage mesh size	117984	238950	449735
outlet mesh size	71280	115200	177600
y^+ on blades min-max	1.67-42	1.4-25.3	1.3-14.1
y^+ area average value on blades	15.4	11.6	11.3
first node from wall [µm]	92	42	23
H [m]	35.18	35.1	35.1

(a)
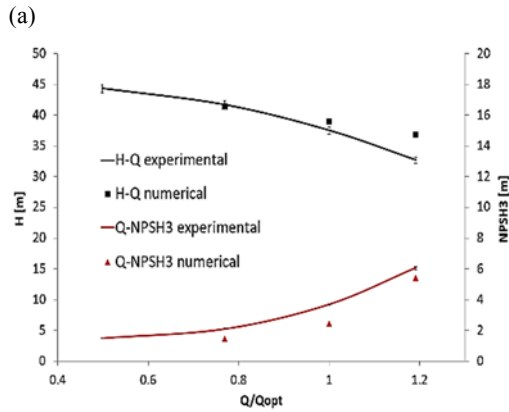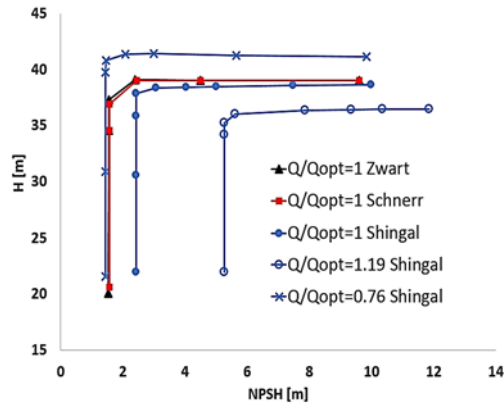
(b)

Fig. 12. Head-drop (a) Q-H and Q-NPSH₃ (b) curves of n_s = 22.4 pump.

(a)
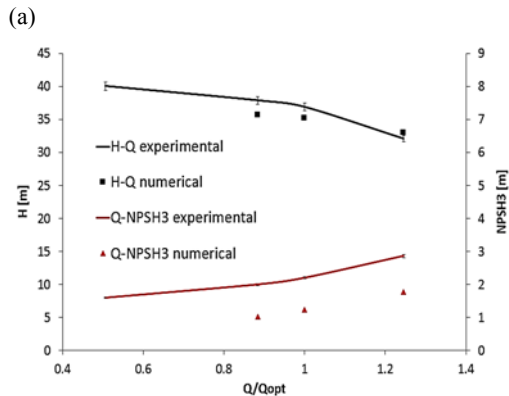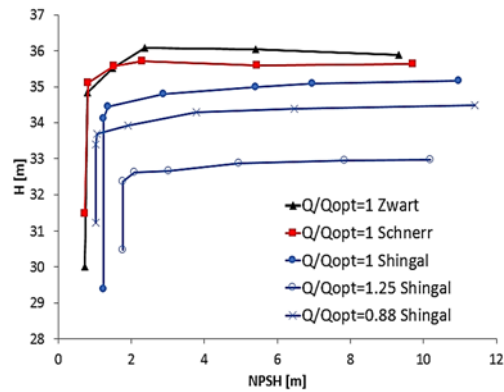
(b)

Fig. 13. Head-drop (a) Q-H and Q-NPSH₃ (b) curves of n_s = 10.4 pump.

A coarse mesh is selected in this case because the calculated head variation is only 0.2% with a finer mesh.

Head-drop curves are calculated in a similar manner in reference to other pump calculations (see Fig. 13a). The head breakdown and $NPSH_3$ values computed with the Zwart and Schnerr models are similar. The highest $NPSH_3$ value at BEP is calculated using the Singhal model, like other two pumps. Because the most accurate results at BEP are calculated using the Singhal model, this model is used to compute the cavitation at off-design operating points. Steep head-drop curves are obtained at all operating points.

The Q-$NPSH_3$ curves are constructed using Fig. 13a. It is seen that the calculated $NPSH_3$ is lower than the experimental values over the operating range of the pump (see Fig. 13b). A maximum $NPSH_3$ calculation error of 48% is revealed at partload operating point, resulting in a 1.08 m absolute difference.

5. CONCLUSIONS

The capabilities of three homogeneous mixture cavitation models are investigated in three radial flow pumps with different specific speeds. Cavitation performances of the pumps are calculated for BEP and off-design operating points, and compared to experimental data based on the $NPSH_3$ measurements. It is observed that the numerical results using the Singhal cavitation model are more accurate than other models in the selected radial pump range. Using the Singhal model, the $NPSH_3$ calculation error is within the limits of the NPSH margin. However, there are stability issues associated with this model. When the vapor volume fraction exceeds a certain limit, the pressure and mass flow rates oscillate excessively at the inlet and outlet. Residuals for the volume fraction equation do not drop below 10^{-4} in several cases. In contrast, the other models are more robust and converge quickly. It is highly recommended to use these models after the parametric optimization of the model coefficients is performed.

The cavitating flow of the n_s = 34.4 pump is simulated incorporating all the rotating and stationary elements, including the leakage patterns, balance holes, and seal flush. It is observed that the head-drop curves do not deviate significantly from the single passage calculations at BEP. Therefore, passage calculations under periodic BCs are recommended for a faster generation of the head-drop curves.

The effect of inlet and outlet BCs on the cavitation performance curves are analyzed using three cavitation models. Mass flow inlet and static pressure outlet boundary conditions provided satisfactory results using the Singhal model. A mass flow outlet BC with zero vapor volume fraction leads to an unrealistic head-drop curve, and should therefore be prevented. However, the head-drop curves do not change when using the Zwart and Schnerr models with the modified BC set.

For all the cases, NPSH$_3$ is estimated to be lower than the experimental values. The possible reasons include the following:

1. Usage of the turbulence model without any modification for multiphase flow: Bubbles form when the local pressure falls below the vapor pressure. The main reason for the pressure drop in a pump is the acceleration of the fluid around the suction side of the blade near the leading edge. In this study, cavitation is calculated in the allowable operating region of the pump. Owing to shockless entry conditions, low-momentum fluid accumulates at the separated flow field under adverse pressure gradient. Bubbles form and grow in these low-pressure fields and collapse downstream. In order to calculate appropriately the separated flow field, realizable k–ε turbulence model with scalable wall functions is used. Because turbulence models are constructed for single-phase flow, Coutier-Delgosha *et al.* (2003) proposed a correction for the turbulent viscosity for unsteady cavitation calculations. This correction is successfully applied in the recent study of Tran *et al.* (2015) for the hydrofoil case and by Zhang *et al.* (2015) for the centrifugal pump case. However, in this work, the turbulence model is used in its original form. A reduction of the turbulent viscosity will enhance cavitation.

2. The non-condensable gas content of experiment water: The mass fraction of dissolved air is not measured. Future studies will be conducted for the gas content influence on the cavitation performance for the same series of pumps.

3. Utilization of the MRF scheme with a steady state approach, which eliminates all the transient effects: Sometimes, a transient analysis is required to calculate even the Q–H characteristics correctly. However, transient cavitation calculations make it unpractical for industry, due to the huge costs of calculation time.

REFERENCES

Balasubramanian, R., E. Sabini and S. Bradshaw (2011). Influence of impeller leading edge profiles on cavitation and suction performance. Proceedings of the 27th Int. Pump Users Symp. , Houston, Texas.

Coutier-Delgosha, O., R. Fortes-Patella and J. L. Reboud (2003). Evaluation of the turbulence model influence on the numerical simulations of unsteady cavitation. Journal of Fluids Engineering 125, 38-45

Ding, H., F. C. Visser, Y. Jiang and M. Furmanczyk (2011). Demonstration and validation of a 3D CFD simulation tool predicting pump performance and cavitation for industrial applications. Journal of Fluids Engineering 133, 011101-1-14.

Dupont, P. (2001). Numerical prediction of the cavitation in pumps. Proceedings of the 18th Int. Pump Users Symp., Houston, Texas.

Hirschi, R., P. Dupont, F. Avellan, J. N. Favre, J. F. Guelich and E. Parkinson (1998). Centrifugal pump performance drop due to leading edge cavitation numerical predictions compared with model tests. Journal of Fluids Eng. 120, 705-711

Jeanty, F., J. De Andrade, M. Asuaje, F. Kenyery A. Vasques, O. Aguillon and A. Tremante (2009). Numerical simulation of cavitation phenomena in a centrifugal pump. Proceedings of the ASME FEDSM2009, Vail, Colorado.

Li, W. G. (2014). Validating full cavitation model with an experimental centrifugal pump. Task Quarterly 18(1), 81-100.

Marini, A., S. Salvadori, C. Bernardini, M. Insinna, F. Martelli, A. Nicchio and A. Piva (2011). Numerical prediction of cavitation inception in centrifugal impellers. Proceedings of the 9th European Conference on Turbomachinery, Istanbul, Turkey.

Niedzwiedzka, A., G. H. Schnerr and W. Sobieski (2016). Review of numericals models of cavitating flows with the use of homogeneous approach. Archives of Thermodynamics 37(2), 71-88

Nohmi, M. (2012). A review a basic research on total prediction system for cavitation phenomena. Proceedings of the 8th Int. Symp. on Cavitation, Singapore.

Schnerr, G. H. and J. Sauer (2001). Physical and numerical modeling of unsteady cavitation dynamics. Proceedings of the 4th ICMF, New Orleans, USA

Shukla, S. N. and J. Kshirsagar (2008). Numerical prediction of cavitation in model pump. Proceedings of the IMECE2008, Boston, Massachusetts.

Singhal, A. K., Athavale, M. M., H. Li and Y. Jiang (2002). Mathematical basis and validation of the full cavitation model. Journal of Fluids Eng. 124, 617-624.

Tran, T. D., B. Nennemann, T. C. Vu and F. Guibault (2015). Investigation of cavitation models for steady and unsteady cavitating flow simulaion. Int. J. of Fluid Mac. and Sys. 8(4), 240-253.

Visser, F. C. (2001). Some user experience demonstrating the use of CFD for cavitation analysis and head prediction of centrifugal pump. Proceedings of the 4th ASME Int. Symp. on Pumping Mach., New Orleans, Louisiana.

Wang, Y.C., Brennen, C.E. (1998) One-Dimensional Bubbly Cavitating Flows Through a

Converging-Diverging Nozzle. ASME J. Fluids Eng. 120, 166–170.

Zhang, D., W. Shi, D. Pan and M. Dubuisson (2015). Numerical and experimental investigation of tip leakage vortex cavitation patterns and mechanisms in an axial flow pump. Journal of Fluids Engineering 137, 121103-1-14

Zwart, P. J., A. G. Gerber and T. Belamri (2004). A two-phase flow model for predicting cavitation dynamics. Proceedings of the 5th ICMF, Yokohama.